energies

MDPI

Article

Comparative Porosity and Pore Structure Assessment in Shales: Measurement Techniques, Influencing Factors and Implications for Reservoir Characterization

Yujie Yuan * and Reza Rezaee

Western Australian School of Mines, Minerals, Energy and Chemical Engineering, Curtin University, Perth, WA 6845, Australia; R.Rezaee@curtin.edu.au
* Correspondence: yujie.yuan@postgrad.curtin.edu.au

Received: 9 May 2019; Accepted: 29 May 2019; Published: 31 May 2019

Abstract: Porosity and pore size distribution (PSD) are essential petrophysical parameters controlling permeability and storage capacity in shale gas reservoirs. Various techniques to assess pore structure have been introduced; nevertheless, discrepancies and inconsistencies exist between each of them. This study compares the porosity and PSD in two different shale formations, i.e., the clay-rich Permian Carynginia Formation in the Perth Basin, Western Australia, and the clay-poor Monterey Formation in San Joaquin Basin, USA. Porosity and PSD have been interpreted based on nuclear magnetic resonance (NMR), low-pressure N_2 gas adsorption (LP-N_2-GA), mercury intrusion capillary pressure (MICP) and helium expansion porosimetry. The results highlight NMR with the advantage of detecting the full-scaled size of pores that are not accessible by MICP, and the ineffective/closed pores occupied by clay bound water (CBW) that are not approachable by other penetration techniques (e.g., helium expansion, low-pressure gas adsorption and MICP). The NMR porosity is largely discrepant with the helium porosity and the MICP porosity in clay-rich Carynginia shales, but a high consistency is displayed in clay-poor Monterey shales, implying the impact of clay contents on the distinction of shale pore structure interpretations between different measurements. Further, the CBW, which is calculated by subtracting the measured effective porosity from total porosity, presents a good linear correlation with the clay content ($R^2 = 0.76$), implying that our correlated equation is adaptable to estimate the CBW in shale formations with the dominant clay type of illite.

Keywords: gas shale; NMR; helium porosimetry; clay bound water; porosity; pore size distribution; low-pressure gas adsorption; MICP

1. Introduction

The increasing demand of unconventional energy resources raises the significance of shale reservoir investigation [1,2]. Shales are defined as the laminated fine-grained argillaceous sedimentary rock, which are essentially constituted by minerals involving silt-sized particles (4–62.5 µm) and clays (<4 µm) in couple with organic matter (OM) [3–6]. The porosity and pore size distribution (PSD), performing as the most fundamental pore structure parameters to estimate gas storage capacity and fluid transporting behaviour in shale complex pore structures [4,7–9], are significantly associated with clay minerals and the promising OM that significantly varies between different shale formations [10–14]. The clay mineral or OM develops the micropore (i.e., pores smaller than 2 nm per International Union of Pure and Applied Chemistry (IUPAC) classification [15]) and mesopore (i.e., pores ranging from 2 nm to 50 nm per IUPAC classification [15]) system, complicating shale pore structures and resulting in the extremely low permeability, low porosity and the large distinction of PSD in shales.

To date, three types of laboratory techniques are applied for pore characterization or quantification. Microscopy techniques, e.g., transmission electron microscopy (TEM) and scanning electron microscopy (SEM), perform as the helpful petrographic-imaging approaches for porosity estimation [16], however, provide objective results and are not adaptable to cover the full range of PSD in shales [12]. Radiation Scatterings, such as small angle neutron scattering (SANS) and ultra-small angle scattering (USANS) techniques, are capable to quantify the continuous PSD in tight sandstones [17] and coals [18,19]. However, the applications in shale systems are still under debate due to the limitation of neutron sources [2,20–22]. Fluid penetration methods, i.e., low-pressure (<18.4 psi) CO_2 gas adsorption (LP-CO_2-GA), low-pressure N_2 gas adsorption (LP-N_2-GA), mercury intrusion capillary pressure (MICP) and nuclear magnetic resonance (NMR), enable a wide range of pore structure detection and have been universally utilized in shale research studies [23–31]. However, MICP displays destructive disadvantages and is not approachable to the pore throat sizes smaller than 3.6 nm [3,11,32,33], merely inter-communicated pores are available for detection [34]. Helium expansion is attainable to the connected pore space corresponding to effective porosity, while the acquisition of PSD is not available [7]. LP-CO_2-GA coupled with LP-N_2-GA is approachable to the pore sizes ranging from 0.35 nm to 200 nm [35]. However, only interconnected pores are accessible [34], and the results are sensitive to measurement procedures and highly dependent on the sample pre-treatment such as the dewatering/ outgassing temperatures and the size of the smashed shale fragments [36–38]. NMR, which is acknowledged as a non-destructive technique, is adaptable for measuring the total porosity and PSD in shales [4,27,39–41].

Unlike the conventional rocks displaying consistent results in porosity and PSD among different fluid-penetration measurements [42], shales, however, tend to reveal significant discrepancies. For example, MICP porosity in Barnett shales exhibit ~25–50% lower when compared to helium porosity values [43]. Similar porosity inconsistencies up to 50% have also been found in previous studies [32,44,45]. To fully understand the variations of shale pore structure interpretation between different measurements, the comprehensive techniques are highly required to be combined and compared in parallel.

This paper discusses the discrepant results of different measurements for the two shales in typical composition (i.e., the Carynginia shales of the Perth Basin in Western Australia and the Monterey shales of San Joaquin Basin in the U.S). Porosity is compared based on MICP, NMR and helium expansion. PSD is interpreted based on MICP, NMR, and low-pressure gas adsorption. The influencing factors are discussed for result discrepancies. Implications are provided for shale gas reservoir characterization.

2. Materials and Methods

2.1. Shale Samples

Shale samples from two formations were analyzed and compared between different measuring techniques. Carynginia samples, by the name of "AC1-AC8", were collected from Arrowsmith well in the Perth Basin, Western Australia. Monterey shales, by the name of "M1-B-M10-B" and "M1-M6", came from well-1B and well-1, respectively, in the San Joaquin Basin, USA. Geological settings of Carynginia and Monterey shale formation were displayed in other studies [27,46].

Table 1 shows the mineralogical composition in Carynginia and Monterey shales. Carynginia shales are characterized by abundant clay minerals, constituting 31.1–50.8 wt % of the total mineral contents (e.g., the average value of Carynginia clay content is 36.6 wt %). The quartz contents occupy 35.6–53.2 wt % (e.g., quartz averages in 45.17 wt %), while the minorities are shown in K-feldspar, plagioclase and other minerals. Monterey shales present a low-clay content (e.g., the mean value of the clay content is around 9.0 wt %) but a relatively high proportion in quartz content. The clay type in both of Carynginia and Monterey shales have been identified as illite [27,47].

Table 1. XRD mineralogical composition for shales from Caryngingia and Monterey formation. Some data were collected from the other studies.

Name	Formation	Depth (m)	Total Clay (wt %)	Quartz (wt %)	K-Feldspar (wt %)	Plagioclase (wt %)	Other Minerals (wt %)
AC1	Caryngingia	2780.2	50.8	35.6	2.6	5.0	6.0
AC2	Caryngingia	2781.7	43.2	40.3	3.6	7.6	5.3
AC3	Caryngingia	2789.9	32.3	47.6	5.4	9.4	5.3
AC4	Caryngingia	2794.4	31.1	53.0	3.3	8.1	4.5
AC5	Caryngingia	2806.4	40.7	41.3	3.6	7.6	6.8
AC8	Caryngingia	2825.3	32.3	53.2	1.4	10.6	2.5
M1-B [47]	Monterey	1633.7	7.3	83.6	1.6	0.7	6.8
M2-B [47]	Monterey	1658.1	4.9	55.2	0.0	0.5	39.4
M3-B [47]	Monterey	2409.7	11.1	59.2	4.1	1.8	23.8
M4-B [47]	Monterey	2539.9	6.8	77.5	2.2	1.3	12.2
M5-B [47]	Monterey	2602.7	N/A	N/A	N/A	N/A	N/A
M6-B [47]	Monterey	2631.0	24.2	50.4	3.3	5.2	16.9
M7-B [47]	Monterey	2723.4	8.4	77.0	2.5	1.8	10.3
M8-B [47]	Monterey	2772.8	8.5	71.0	1.4	3.3	15.8
M9-B [47]	Monterey	2802.0	14.7	72.6	2.2	3.6	6.9
M10-B [47]	Monterey	2879.4	5.6	10.6	0.0	0.0	83.8
M1 [47]	Monterey	1669.5	N/A	N/A	N/A	N/A	N/A
M2 [47]	Monterey	2200.9	10.0	69.0	4.0	6.0	11.0
M3 [47]	Monterey	2203.2	N/A	N/A	N/A	N/A	N/A
M4 [47]	Monterey	2362.4	N/A	N/A	N/A	N/A	N/A
M5 [47]	Monterey	2362.7	N/A	N/A	N/A	N/A	N/A
M6 [47]	Monterey	2485.3	7.0	68.0	5.0	6.0	14.0

2.2. Nuclear Magnetic Resonance (NMR)

Prior to NMR experiments, Caryngingia shale plugs of 1.5′ diameter were cleaned with toluene/methanol mixture, and fully saturated with 30,000 ppm brine that are matched with the average formation salinity. The low-field NMR measurements were performed on saturated samples by using 2 MHz Magritek Rock Core Analyzer, which was set under 30°C with P54 probe and conducted under the constant magnetic resonance frequency. NMR T_2 spectrum was acquired by using the experimental parameters, i.e., 100 µs inter-echo spacing (TE), 10,000 ms inter-experiment delay, 10,000 number of echoes and the minimum 200 signal to noise ratio (SNR), coupled with the Carr-Purcell-Meilboom-Gill sequence [48–50].

Applying NMR T_2 spectrum to study shales pore structure is fundamentally established on the transverse relaxation dominated by surface relaxation mechanism [39]:

$$\frac{1}{T_2} = \rho_2\left(\frac{S}{V}\right) \tag{1}$$

where T_2 is the transverse relaxation time; ρ_2 is surface relaxivity, which is considered as a constant value representing the strength of surface relaxation; $\frac{S}{V}$ is the surface volume ratio that is closely intimated with pore sizes. Pore size distribution could be interpreted via T_2 spectrum, with smaller pore sizes corresponding to shorter relaxation times.

2.3. Low-Pressure Gas Adsorption (LP-GA)

Low-pressure N_2 gas adsorption (LP-N_2-GA) was applied to measure the pore size distribution (PSD) and the pore volume. Prior to the measurements, shale samples were crushed into fragments of 60 mesh sizes and degassed over 8h for pore surface cleaning. LP-N_2-GA was performed on Micromeritics® TriStar 3020 instrument at the bathing temperature of 77.4 K. N_2 was penetrated into the degassed samples under the constant temperature for the acquisition of adsorption isotherm. PSD is obtained by using the Barrett, Joyner and Halenda (BJH) theory based on N_2 adsorption isotherm [35]. The interpretations were carried out on the embedded TriStar II 3020 standard software.

2.4. Mercury Injection Capillary Pressure (MICP)

MICP measurements were performed on Micromeritics Autopore IV 9500 V1.09 porosimeter on chip samples weighing around 10 g. Prior to the test, shale chips were evacuated under the pressure of 70 µmHg for 10 min. The non-wetting mercury, as the working probe for pore access, follows the parameters applied as: Hg density of 13.53 g/mL; adv. and rec. contact angle of 130°; Hg surface tension of 485 dynes/cm. The mercury filling pressure was performed of 0.51 psia under 10 s for equilibration, followed by injection under high pressure, ranging from 0.1 MPa (14.5 psi) to the maximum 413.7 MPa (60,000 psi), which corresponds to the pore throat size from 3.6 nm to 1100 µm.

The pore throat size distribution of tested samples is obtained using Washburn equation assuming cylindrical pores (Equation (2)) [51]:

$$r_i = \frac{-2\sigma \cos\theta}{P_c} \tag{2}$$

where r_i is the pore throat radius calculated under mercury pressure of P_c (psi), µm; σ is the mercury surface tension (485 dynes/cm applied in the test); θ is mercury contact angle (130° applied in the test); p_c is the injection pressure ranging from 14.5 psi to the maximum 60,000 psi.

3. Results

3.1. Porosity

The porosity values obtained from three measuring techniques (i.e., MICP, Helium, and NMR) are shown for two different shale formations (i.e., Carynginia and Monterey) (Figure 1). An obvious porosity distinction is displayed in NMR between the clay-rich samples (i.e., Carynginia) and the clay-poor samples (i.e., Monterey). An overall higher NMR porosities are exhibited in Carynginia compared to Monterey. In addition, the porosity discrepancies are apparently exhibited between NMR and the other two measurements in Carynginia samples. Carynginia presents the highest porosity value in NMR, which is more than two times as MICP porosity, and about three times as helium porosity (i.e., the porosity measured by NMR, helium, and MICP ranges in 8.02–12.87%, 3.03–3.78%, and 1.93–4.15%, respectively). However, the Monterey exhibits a high porosity consistency in NMR, helium and MICP (Figure 1). The porosity measured from MICP and helium demonstrates high consistencies in both Carynginia and Monterey. As shown in Figure 2, the cross-plot of helium porosity versus MICP porosity generates a very good positive linear relationship, with the correlation coefficient (R^2) of 0.93. The porosity values for each sample are shown in Appendix A (Table A1).

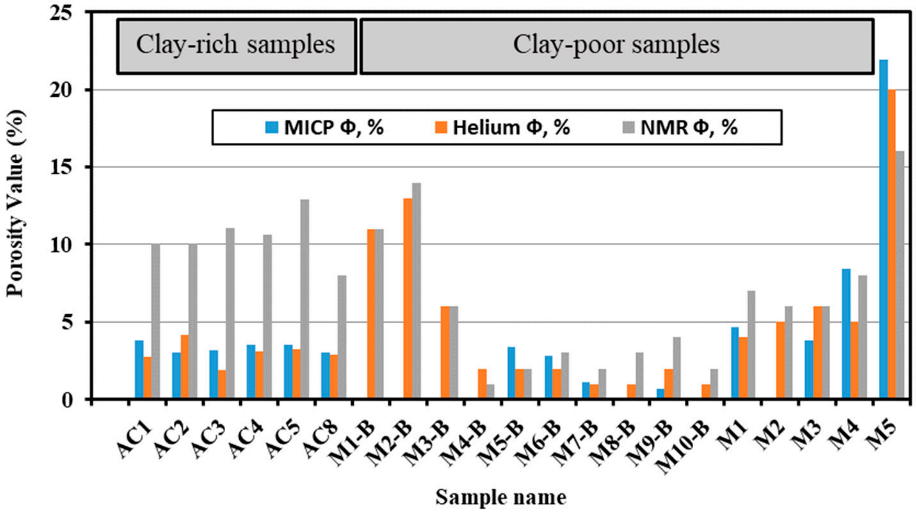

Figure 1. The porosity values obtained from mercury intrusion capillary pressure (MICP), Helium, and nuclear magnetic resonance (NMR) for two different shale formations.

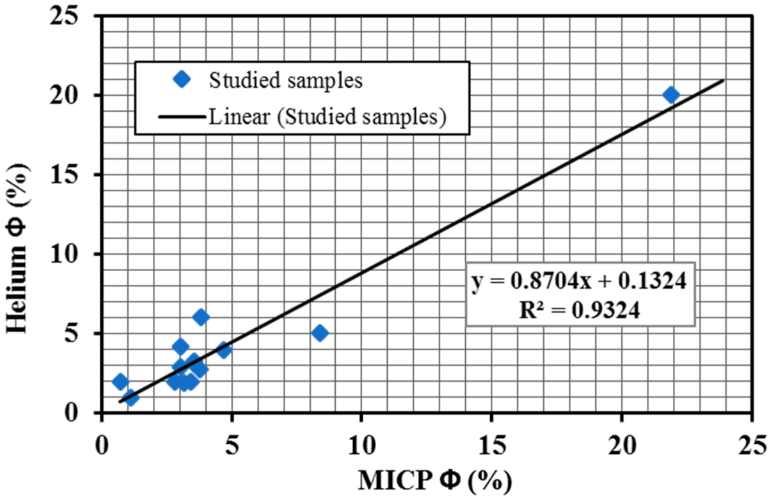

Figure 2. The cross-plot of Helium porosity (%) versus MICP porosity (%) for the studied samples.

3.2. The Pore Size Distribution from NMR

Figure 3 presents the NMR T_2 spectrum in Carynginia shales, with the majority of pores identified in small pore sizes. The peak values of T_2 curves correspond to the T_2 relaxation time around 0.3–1 ms. The samples of higher clay contents, e.g., AC1 and AC2 (i.e., 50.8% and 43.2%), exhibit larger amplitude and narrower spectrum with the peak value locating in smaller pore sizes. The samples of relatively lower clay contents, e.g., AC8 and AC4 (i.e., 32.3% and 31.1%), display smaller amplitude and wider distributions, presenting a general larger pore sizes. A uniform pore size distribution is commonly indicated in Carynginia shales.

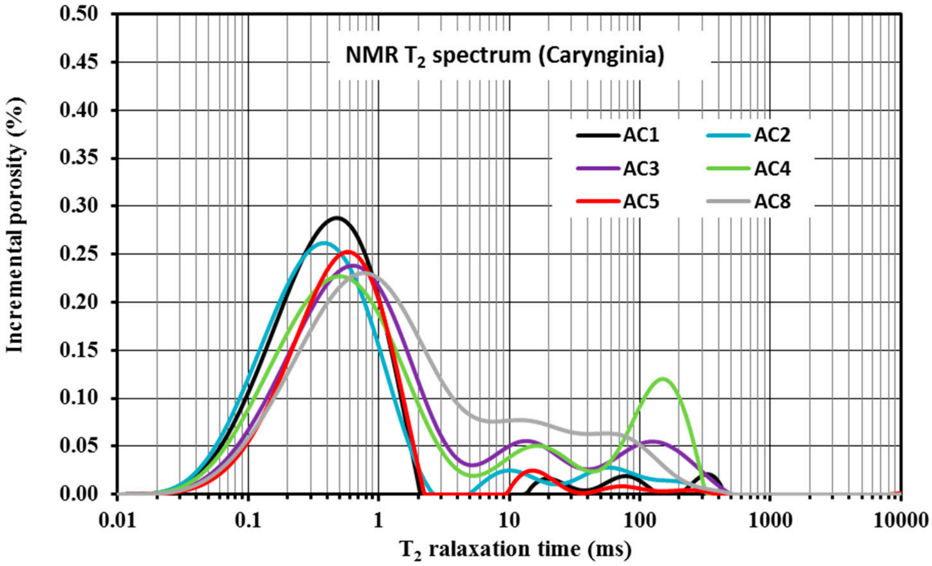

Figure 3. NMR T_2 spectrum for Carynginia shales (i.e., AC1-AC8).

NMR T_2 spectra of Monterey shales, i.e., M1-M6 and M1-B-M10-B, are displayed in Figures 4 and 5, respectively. Significant variations are demonstrated in Monterey shales compared to Carynginia shales. As shown in Figure 4, Monterey shales from Well 1 (except for M5) exhibit the major pores in larger pore size ranges. The peak locations of the spectrum correspond to T_2 relaxation time ~1–100 ms, coupled with an overall wider spectrum range, indicating a general uneven pore size distributions. The peak values (except for M5) correspond to the incremental porosity between 0.1% and 0.13%, displaying overall lower values than that in Carynginia shales. M5 shows the trimodal spectrum associated with three typical pore types. The spectrum peak of M5 occurs at T_2 relaxation time in 300–500 ms, representing the majority of larger pores or fractures.

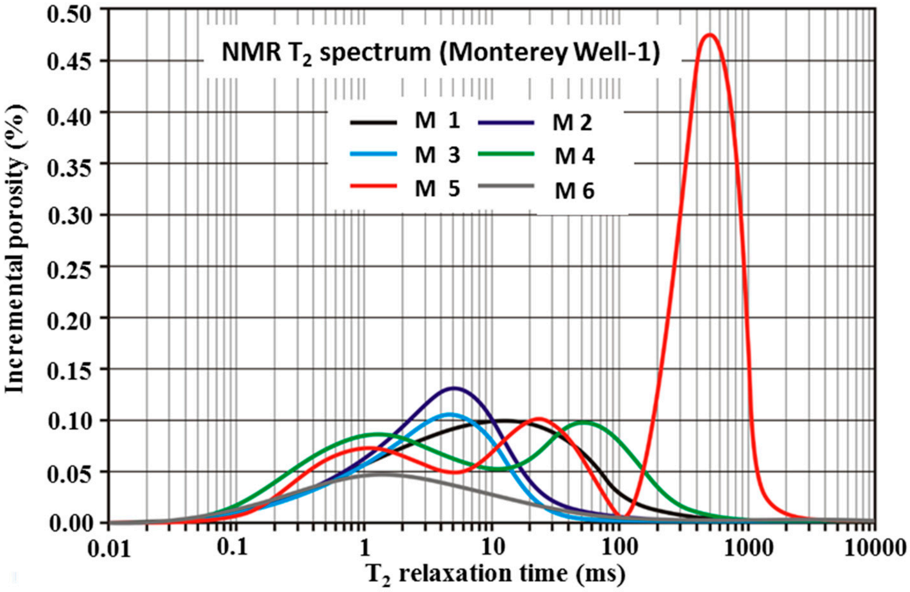

Figure 4. NMR T_2 spectrum for Monterey shales (i.e., M1–M6) collected from Well 1. Modified from Rivera [46].

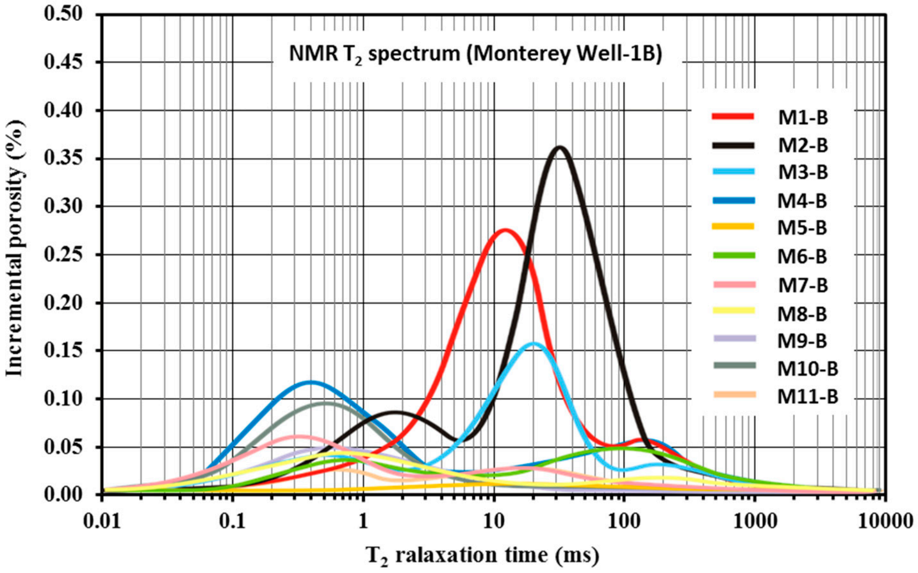

Figure 5. NMR T_2 spectrum for Monterey shales (i.e., M1-B–M6-B) collected from Well 1B. Modified from Rivera [46].

Figure 5 shows the T_2 spectrum of Monterey shales from Well 1B with multiple modal types. M4-B, M10-B, M7-B, M9-B exhibit a majority of small pore sizes, corresponding to the T_2 relaxation times of ~0.3–1 ms. M1-B and M2-B with semi-modal distributions present the PSD peaks at larger T_2 relaxation time (i.e., 14 ms and 40 ms respectively) and higher incremental porosity (i.e., 0.27% and 0.36% respectively). M3-B exhibits trimodal spectrum with the main pore size locates at ~20 ms. When compared to T_2 spectrum in clay-rich Caryngina, the pore sizes in Monterey are rather unevenly distributed and universally locating in larger pore sizes. Moreover, unlike Caryngina, no obvious correlations are observed between the clay contents and the NMR PSD amplitudes in Monterey shales.

3.3. The Pore Size Distribution from Gas Adsorption

Figure 6 displays Caryngina PSD obtained from LP-N_2-GA experiments. As can be seen, the PSD peak in Caryngina appears around 20 nm, implying the pore majority locating in fine mesopore sizes that dominantly controls the total pore volume. Monterey shales, by contrast, present a different scenario (Figure 7), showing PSD peak at ~50–100 nm with the pore majority in fine macropore ranges, which is intimately related to the high quartz content.

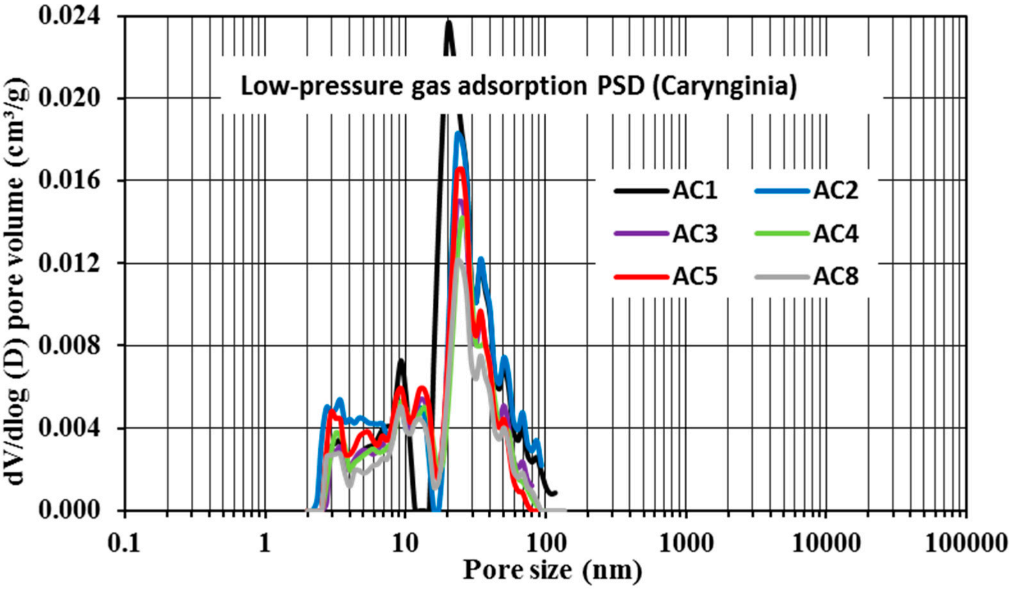

Figure 6. Caryngina pore size distribution (PSD) derived from low-pressure N_2 gas adsorption based on BJH theory.

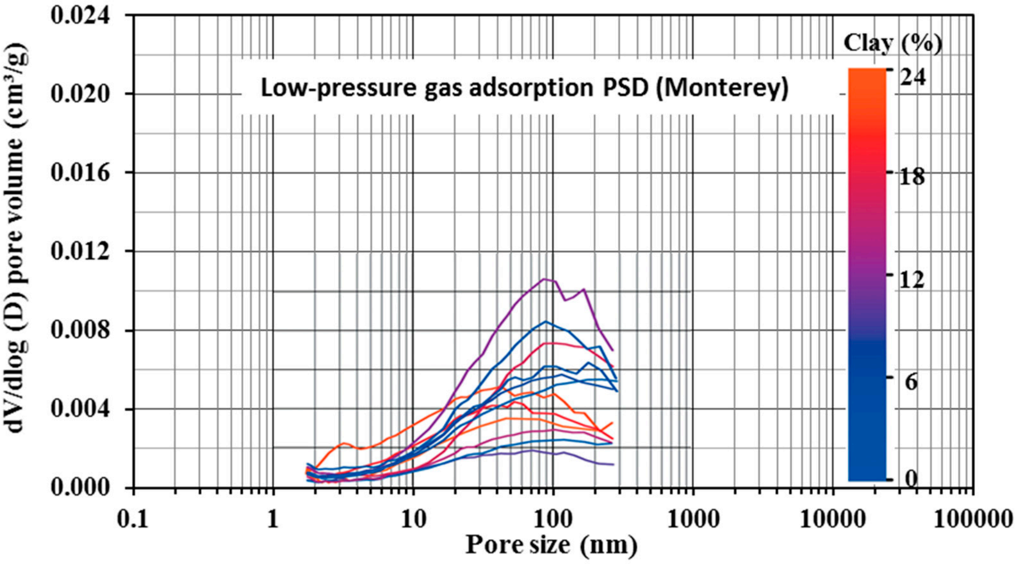

Figure 7. Monterey pore size distribution (PSD) derived from low-pressure N_2 gas adsorption. Modified from Saidian, Kuila [44].

3.4. The Pore Throat Size Distribution from MICP

Caryngina and Monterey pore throat size distributions (PTDs) measured by MICP are plotted in Figures 8 and 9. The peaks of MICP- derived PTD in Caryngina are commonly located in pore sizes ~4–5 nm, which are smaller compared to that interpreted by LP-N_2-GA. A wider range of the detectable large pores (i.e., pore sizes larger than 100 nm) is revealed by MICP technique compared to LP-N_2-GA. Consistent with the NMR and LP-N_2-GA interpretations for Carynginia samples, larger PTD amplitude is shown in the samples of higher clay (e.g., AC1, AC2), while the lowest PTD amplitude is found in samples of the lowest clay samples (i.e., AC8). The Monterey PTD, however, presents a weak interrelationship between the clay content and the amplitude of curve (Figure 9), which agrees with the behaviours of Monterey PSD (e.g., Figures 4, 5 and 7) that is most likely under the large influences of low-clay contents [44].

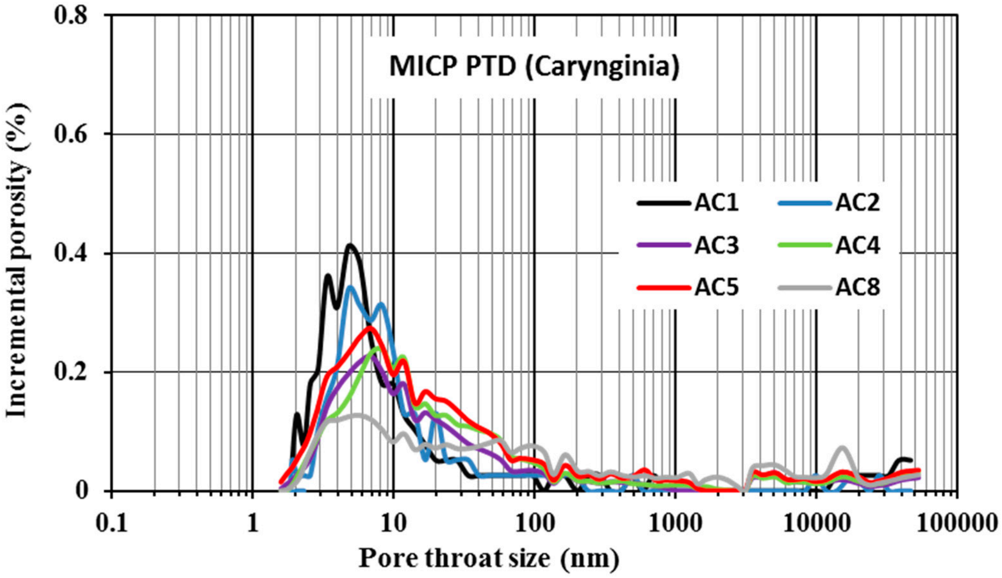

Figure 8. MICP pore throat size distribution (PTD) for Permian Carynginia shales.

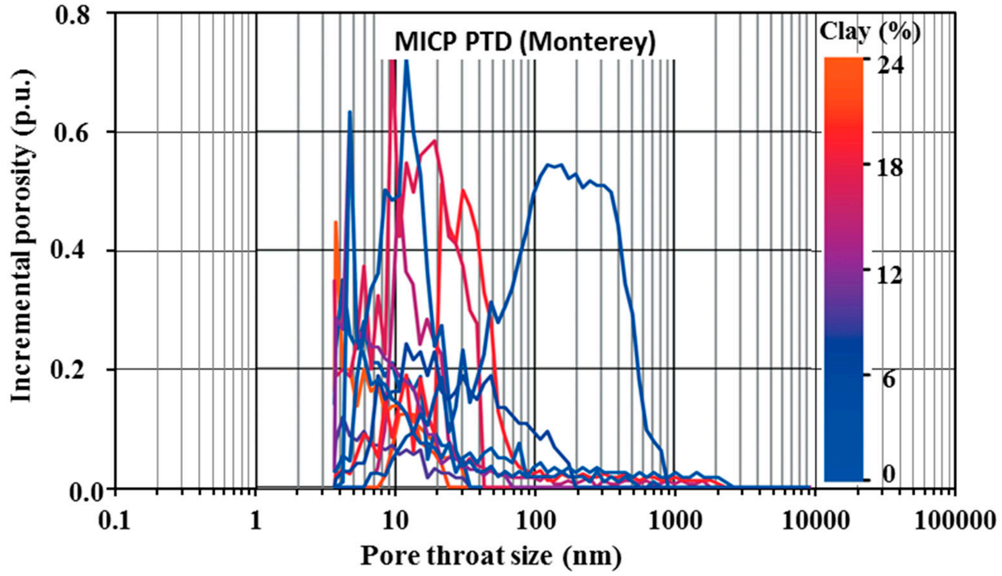

Figure 9. MICP pore throat size distribution (PTD) for Monterey shales. Modified from Saidian, Kuila [44].

4. Discussion

Carynginia samples are characterized by abundant clay contents, while Monterey shales are clay-poor (Table 1). NMR technique, which is highlighted by non-destructive measurement of total porosity, involves the detection of effective porosity and clay bound water (CBW), which is tightly bound on the surface area of clay minerals and universally quantified by cutting the effective porosity off total porosity [52,53]. Other penetration approaches, e.g., helium, MICP, and low-pressure gas adsorption, nevertheless, are merely approachable to the inter-connected pores, missing out the closed-pores or the ineffective porosity occupied by CBW. Under extreme circumstances, for shales containing very high clay contents and thus high CBW, the most of pore spaces could be nearly fully-occupied by the volume of CBW [8,54] that would influence the petrophysical properties in shales [27,55–57]. As helium porosimetry is able to obtain effective porosity by covering a wider pore size range (i.e., 0.1 nm–100 μm) than MICP (i.e., 3.6 nm–100 μm) (Figure 10) [34], the CBW is calculated by subtracting the helium porosity (i.e., effective effective) from NMR porosity (i.e., total porosity). Figure 11 cross-plots the calculated CBW versus the clay content in both Carynginia and Monterey shales. The CBW, which accounts for the porosity discrepancy between NMR and helium measurement, displays higher values in clay-rich Caryngnia shales, but lower values are found in Monterey shales. The correlation presents a good linear relationship ($R^2 = 0.76$), indicating that the correlation equation (Equation (3)) is adaptable for the estimation of CBW in the shale, whose clay type is dominantly contributed by illite:

$$CBW\ (\%) = 0.19\ \times V_{sh}\ (\%) - 0.7 \tag{3}$$

where CBW is the volume of clay bound water (%), V_{sh} (%) is the clay contents (%). Moreover, the equation is most likely to fit into the formation with the brine salinity of 20,000–30,000 ppm that matches with our studied formations.

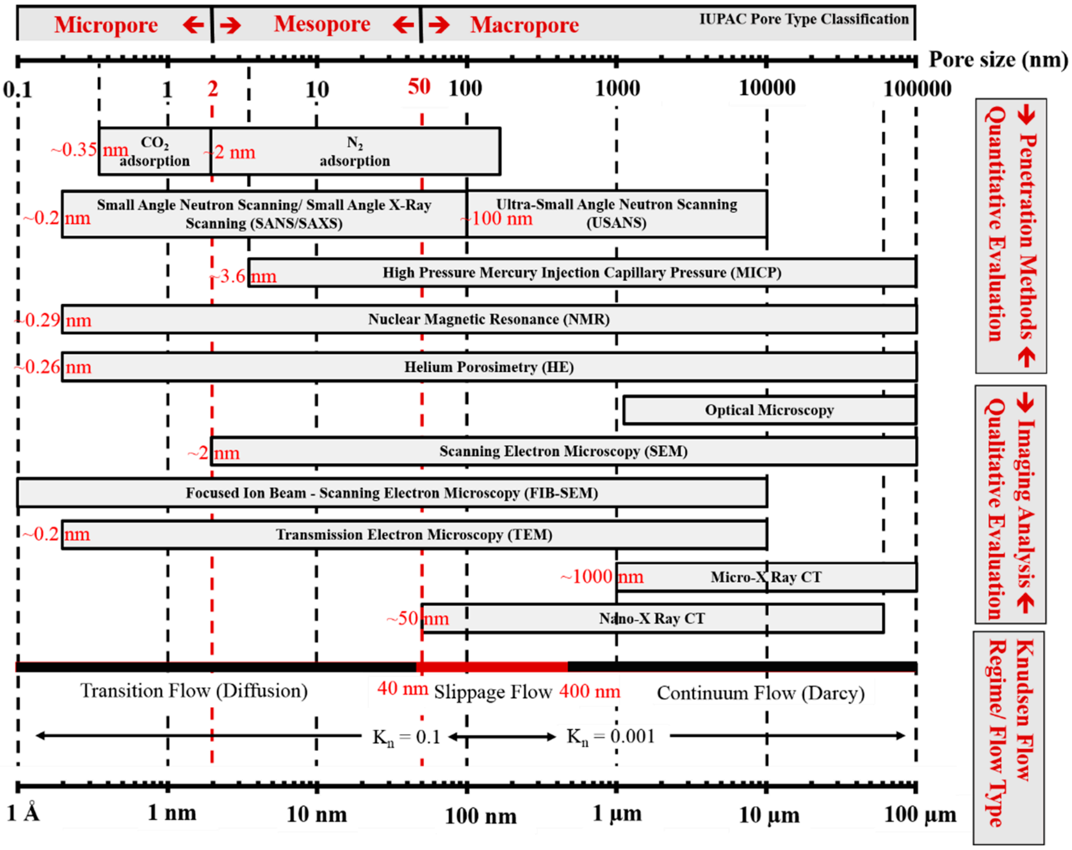

Figure 10. The multi-scaled methods for pore characterization in shales Modified from other studies [32,34,58,59].

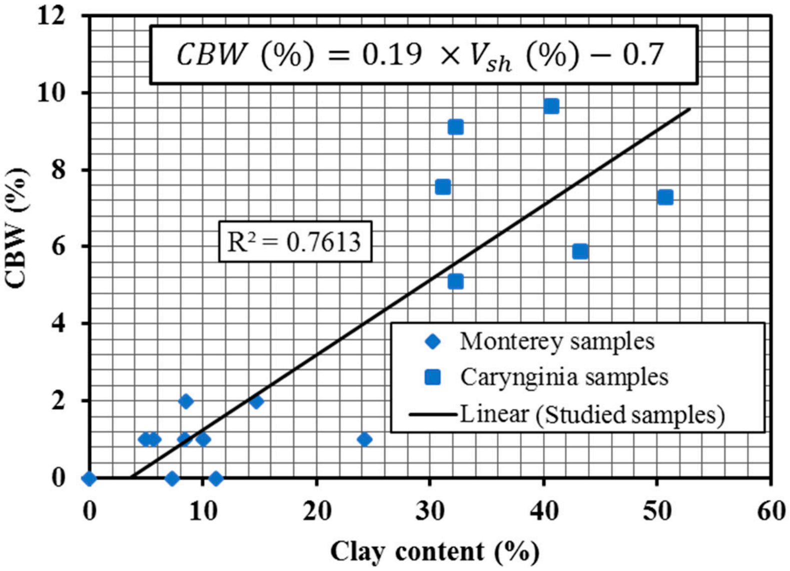

Figure 11. The cross-plot of clay bound water (CBW) (%) versus clay content (%) for studied shale samples.

Apart from the influencing factors associated with clays, the compatibility of the penetrated working fluid molecules with shale nanopore structure also causes the interpretation inconsistencies. Unlike NMR using H_2O as working fluid to access pore body, the working molecule involved in MICP is merely attainable to the limited pore throat size. The mineral-controlled geometrical pore shapes, which are highly intimated with the mineral compositions and assemblages, pose a large impact on the porosity discrepancies between NMR and MICP in Caryngnia shales [60]. To summarize, the possible reasons for the higher NMR porosity over MICP are: (1) the volume of clay bound water; (2) the porosity contributed by pores smaller than 3.6 nm; (3) the different mechanisms involved in NMR pore body detection versus MICP pore throat detection (e.g., MICP assumes the pores are cylindrical in shape with a smooth surface, but the real pores are complicated with rough surfaces bound with water layers) [34]; (4) the pore shape combination that intimately related to shale compositions. When the comparisons are carried out between helium and MICP, theoretically, for shales containing high proportion of micropores, helium porosity is supposed to be higher than MICP due to its wider detection of pore size range [58]. However, the higher MICP porosity values are observed in some of the studied samples in both Caryngnia and Monterey (e.g., AC1, AC3, M5-B, M4) (Figure 1). As the samples from both formations show a small proportion of micropores, the possible reasons could be explained by the increased mercury uptake induced by the high-pressure application (i.e., 60,000 psi) in MICP measurement [61]. Similar phenomenons have also been found in coals [62], which possess similar characteristics as shales [63,64].

5. Conclusions

The discrepancies in porosity or pore size distribution between MICP, NMR, and LP-GA porosimetry are largely controlled by shale compositions, particularly, the clay minerals. The clay-rich shales generate NMR porosity significantly higher than MICP and helium porosity, while the clay-poor shales exhibit a high porosity consistency between NMR, MICP and helium porosimetry.

The higher porosity values unveiled by NMR over MICP/helium technique are fundamentally attributed to CBW, meanwhile, the clay mineral compositions and assemblages, coupled with pore geometry also contribute to the discrepancies. The MICP and helium both detect intercommunicated pores and display consistent porosity for shales deficient in pores smaller than 3.6 nm. The shales of deficient micropores may possibly show higher helium porosity over MICP porosity, which essentially result from the high pressure application involved in MICP technique.

Author Contributions: Investigation and writing, Y.Y.; Supervision, reviewing and correcting, R.R.

Funding: This research was funded by China Scholarship Council. Grant number: 201606450018.

Acknowledgments: The authors acknowledge Unconventional Gas Research Group (UGRG), the discipline of Petroleum Engineering and the discipline of Chemical Engineering in Western Australian School of Mines (WASM), Curtin University for the facility assistance. The Department of Mines, Industry Regulation and Safety of the Government of Western Australia is acknowledged for their permission of core sample collections. The editor and anonymous reviewers are also appreciated for their comments to improve this work. Y. Yuan sincerely thanks China Scholarship Council-Curtin International Postgrad Research Scholarship (CSC-CIPRS) for their financial support.

Conflicts of Interest: The authors declare no conflict of interest.

Appendix A

Table A1. The porosity values obtained from MICP, Helium and NMR techniques for the studied samples in Carynginia and Monterey. Some data are collected from other studies [26,27,46].

Name	Formation	Depth (m)	MICP Φ, %	Helium Φ, %	NMR Φ, %
AC1	Carynginia	2780.2	3.78	2.78	10.06
AC2	Carynginia	2781.7	3.05	4.15	10.04
AC3	Carynginia	2789.9	3.17	1.93	11.05
AC4	Carynginia	2794.4	3.54	3.11	10.66
AC5	Carynginia	2806.4	3.56	3.22	12.87
AC8	Carynginia	2825.3	3.03	2.92	8.02
M1-B	Monterey	1633.7	N/A	11.0	11.0
M2-B	Monterey	1658.1	N/A	13.0	14.0
M3-B	Monterey	2409.7	N/A	6.0	6.0
M4-B	Monterey	2539.9	N/A	2.0	1.0
M5-B	Monterey	2602.7	3.4	2.0	2.0
M6-B	Monterey	2631.0	2.8	2.0	3.0
M7-B	Monterey	2723.4	1.1	1.0	2.0
M8-B	Monterey	2772.8	N/A	1.0	3.0
M9-B	Monterey	2802.0	0.7	2.0	4.0
M10-B	Monterey	2879.4	N/A	1.0	2.0
M1	Monterey	1669.5	4.7	4.0	7.0
M2	Monterey	2200.9	N/A	5.0	6.0
M3	Monterey	2203.2	3.8	6.0	6.0
M4	Monterey	2362.4	8.4	5.0	8.0
M5	Monterey	2362.7	21.9	20.0	16.0

References

1. Curtis, J.B. Fractured shale-gas systems. *AAPG Bull.* **2002**, *86*, 1921–1938.
2. Clarkson, C.R.; Solano, N.; Bustin, R.M.; Bustin, A.M.M.; Chalmers, G.R.L.; He, L.; Melnichenko, Y.B.; Radlińskiet, A.P.; Blach, T.P. Pore structure characterization of North American shale gas reservoirs using USANS/SANS, gas adsorption, and mercury intrusion. *Fuel* **2013**, *103*, 606–616. [CrossRef]
3. Chalmers, G.R.; Bustin, R.M.; Power, I.M. Characterization of gas shale pore systems by porosimetry, pycnometry, surface area, and field emission scanning electron microscopy/transmission electron microscopy image analyses: Examples from the Barnett, Woodford, Haynesville, Marcellus, and Doig units. *AAPG Bull.* **2012**, *96*, 1099–1119.
4. Rezaee, R. *Fundamentals of Gas Shale Reservoirs*; John Wiley & Sons: Hoboken, NJ, USA, 2015.
5. Folk, R.L. *Petrology of Sedimentary Rocks*; Hemphill Publishing Company: Cedar Hill, TX, USA, 1980.
6. Javadpour, F. Nanopores and apparent permeability of gas flow in mudrocks (shales and siltstone). *J. Can. Pet. Technol.* **2009**, *48*, 16–21. [CrossRef]
7. Labani, M.M.; Rezaee, R.; Saeedi, A.; Hinai, A.A. Evaluation of pore size spectrum of gas shale reservoirs using low pressure nitrogen adsorption, gas expansion and mercury porosimetry: A case study from the Perth and Canning Basins, Western Australia. *J. Pet. Sci. Eng.* **2013**, *112*, 7–16. [CrossRef]

8. Topór, T.; Derkowski, A.; Kuila, U.; Fischer, T.B.; McCarty, D.K. Dual liquid porosimetry: A porosity measurement technique for oil-and gas-bearing shales. *Fuel* **2016**, *183*, 537–549. [CrossRef]
9. Jia, B.; Tsau, J.-S.; Barati, R. Different flow behaviors of low-pressure and high-pressure carbon dioxide in shales. *SPE J.* **2018**, *23*, 1452–1468. [CrossRef]
10. Sondergeld, C.H.; Ambrose, R.J.; Rai, C.S.; Moncrieff, J. Micro-structural studies of gas shales. In Proceedings of the SPE Unconventional Gas Conference, Pittsburgh, PA, USA, 23–25 February 2010.
11. Mastalerz, M.; Ambroseet, R.J.; Rai, C.S.; Moncrieff, J. Porosity of Devonian and Mississippian New Albany Shale across a maturation gradient: Insights from organic petrology, gas adsorption, and mercury intrusion. *AAPG Bull.* **2013**, *97*, 1621–1643. [CrossRef]
12. Furmann, A.; Mastalerz, M.; Bish, D.; Schimmelmann, A.; Pedersen, P.K. Porosity and pore size distribution in mudrocks from the Belle Fourche and Second White Specks Formations in Alberta, Canada. *AAPG Bull.* **2016**, *100*, 1265–1288.
13. Loucks, R.G.; Reed, R.M.; Ruppel, S.C.; Jarvie, D.M. Morphology, genesis, and distribution of nanometer-scale pores in siliceous mudstones of the Mississippian Barnett Shale. *J. Sediment. Res.* **2009**, *79*, 848–861. [CrossRef]
14. Curtis, M.E.; Cardott, B.J.; Sondergeld, C.H.; Rai, C.S. Development of organic porosity in the Woodford Shale with increasing thermal maturity. *Int. J. Coal Geol.* **2012**, *103*, 26–31. [CrossRef]
15. Rouquerol, J.; Avnir, D.; Fairbridge, C.W.; Everett, D.H.; Haynes, J.M.; Pernicone, N.; Ramsay, J.D.F.; Sing, K.S.W.; Unger, K.K. Recommendations for the characterization of porous solids (Technical Report). *Pure Appl. Chem.* **1994**, *66*, 1739–1758. [CrossRef]
16. Sigal, R.F. Pore-size distributions for organic-shale-reservoir rocks from nuclear-magnetic-resonance spectra combined with adsorption measurements. *SPE J.* **2015**, *20*, 824–830. [CrossRef]
17. Clarkson, C.; Freeman, M.; He, L.; Agamalian, M.; Melnichenko, Y.; Mastalerz, M.; Bustin, R.; Radlinski, A.; Blach, T. Characterization of tight gas reservoir pore structure using USANS/SANS and gas adsorption analysis. *Fuel* **2012**, *95*, 371–385. [CrossRef]
18. Radlinski, A.; Mastalerz, M.; Hinde, A.; Hainbuchner, M.; Rauch, H.; Baron, M.; Lin, J.; Fan, L.; Thiyagarajan, P. Application of SAXS and SANS in evaluation of porosity, pore size distribution and surface area of coal. *Int. J. Coal Geol.* **2004**, *59*, 245–271. [CrossRef]
19. Melnichenko, Y.; Radlinski, A.; Mastalerz, M.; Cheng, G.; Rupp, J. Characterization of the CO2 fluid adsorption in coal as a function of pressure using neutron scattering techniques (SANS and USANS). *Int. J. Coal Geol.* **2009**, *77*, 69–79. [CrossRef]
20. Radlinski, A.P. Small-angle neutron scattering and the microstructure of rocks. *Rev. Mineral. Geochem.* **2006**, *63*, 363–397. [CrossRef]
21. Bahadur, J.; Melnichenko, Y.B.; Radlinski, A.P.; Mastalerz, M.; Schimmelmann, A. Hierarchical pore morphology of cretaceous shale: A small-angle neutron scattering and ultrasmall-angle neutron scattering study. *Energy Fuels* **2014**, *28*, 6336–6344. [CrossRef]
22. Bahadur, J.; Melnichenko, Y.B.; Radlinski, A.P.; Mastalerz, M.; Schimmelmann, A. Small-angle and ultrasmall-angle neutron scattering (SANS/USANS) study of New Albany shale: A treatise on microporosity. *Energy Fuels* **2015**, *29*, 567–576. [CrossRef]
23. Knapp, L.J.; Nanjo, T.; Uchida, S.; Haeri-Ardakani, O.; Sanei, H. Investigating Influences on Organic Matter Porosity and Pore Morphology in Duvernay Formation Organic-Rich Mudstones. In Proceedings of the 24th Formation Evaluation Symposium of Japan, Chiba, Japan, 11–12 October 2018.
24. Kuila, U. *Measurement and Interpretation of Porosity and Pore-Size Distribution in Mudrocks: The Hole Story of Shales*; Colorado School of Mines, Arthur Lakes Library: Golden, CO, USA, 2013.
25. Rezaee, R.; Saeedi, A.; Clennell, B. Tight gas sands permeability estimation from mercury injection capillary pressure and nuclear magnetic resonance data. *J. Pet. Sci. Eng.* **2012**, *88*, 92–99. [CrossRef]
26. Al Hinai, A.; Rezaee, R.; Esteban, L.; Labani, M. Comparisons of pore size distribution: A case from the Western Australian gas shale formations. *J. Unconv. Oil Gas Resour.* **2014**, *8*, 1–13. [CrossRef]
27. Yuan, Y.; Rezaee, R.; Verrall, M.; Hu, S.-Y.; Zou, J.; Testmanti, N. Pore characterization and clay bound water assessment in shale with a combination of NMR and low-pressure nitrogen gas adsorption. *Int. J. Coal Geol.* **2018**, *194*, 11–21. [CrossRef]
28. Ross, D.J.; Bustin, R.M. The importance of shale composition and pore structure upon gas storage potential of shale gas reservoirs. *Mar. Pet. Geol.* **2009**, *26*, 916–927. [CrossRef]

29. Saidian, M.; Godinez, L.J.; Rivera, S.; Prasad, M. Porosity and pore size distribution in mudrocks: A comparative study for Haynesville, Niobrara, monterey, and Eastern European Silurian formations. In Proceedings of the Unconventional Resources Technology Conference, Denver, CO, USA, 25–27 August 2014.
30. Josh, M.; Esteban, L.; Piane, C.D.; Sarout, J.; Dewhurst, D.; Clennell, M. Laboratory characterisation of shale properties. *J. Pet Sci. Eng.* **2012**, *88–89*, 107–124. [CrossRef]
31. Wang, F.; Guo, S. Influential factors and model of shale pore evolution: A case study of a continental shale from the Ordos Basin. *Mar. Pet. Geol.* **2019**, *102*, 271–282. [CrossRef]
32. Sondergeld, C.H.; Newsham, K.E.; Comisky, J.T.; Rice, M.C.; Rai, C.S. Petrophysical Considerations in Evaluating and Producing Shale Gas Resources. In Proceedings of the SPE Unconventional Gas Conference, Pittsburgh, PA, USA, 23–25 February 2010.
33. Nelson, P.H. Pore-throat sizes in sandstones, tight sandstones, and shales. *AAPG Bull.* **2009**, *93*, 329–340. [CrossRef]
34. Caineng, Z.; Songqi, P.; Senhu, L.; Jinliang, H.; Songtao, W.; Dazhong, D.; Shasha, S.; Zhi, Y.; Yanyan, C.; Shufang, W.; et al. Shale Gas Formation and Occurrence in China: An Overview of the Current Status and Future Potential. *Acta Geol. Sin. Engl. Ed.* **2016**, *90*, 1249–1283. [CrossRef]
35. Barrett, E.P.; Joyner, L.G.; Halenda, P.P. The Determination of Pore Volume and Area Distributions in Porous Substances. I. Computations from Nitrogen Isotherms. *J. Am. Chem. Soc.* **1951**, *73*, 373–380. [CrossRef]
36. Holmes, R.; Rupp, E.C.; Vishal, V.; Wilcox, J. Selection of Shale Preparation Protocol and Outgas Procedures for Applications in Low-Pressure Analysis. *Energy Fuels* **2017**, *31*, 9043–9051. [CrossRef]
37. Figini-Albisetti, A.; Velasco, L.F.; Parra, J.B.; Ania, C.O. Effect of outgassing temperature on the performance of porous materials. *Appl. Surf. Sci.* **2010**, *256*, 5182–5186. [CrossRef]
38. Wang, G.; Ju, Y. Organic shale micropore and mesopore structure characterization by ultra-low pressure N 2 physisorption: Experimental procedure and interpretation model. *J. Nat. Gas Sci. Eng.* **2015**, *27*, 452–465. [CrossRef]
39. Coates, G.R.; Xiao, L.; Prammer, M.G. *NMR Logging: Principles and Applications*; Gulf Professional Publishing: Houston, TX, USA, 1999.
40. Morriss, C.; Rossini, D.; Straley, C.; Tutunjian, P.; Vinegar, H. Core analysis by low-field NMR. In *The Log Analyst*; Society of Petrophysicists and Well-Log Analysts: London, UK, 1997; Volume 38.
41. Schön, J.H. *Physical Properties of Rocks: Fundamentals and Principles of Petrophysics*; Elsevier: Amsterdam, The Netherlands, 2015; Volume 65.
42. Hossain, Z.; Grattoni, C.A.; Solymar, M.; Fabricius, I.L. Petrophysical properties of greensand as predicted from NMR measurements. *Pet. Geosci.* **2011**, *17*, 111–125. [CrossRef]
43. Sigal, R.F. Mercury Capillary Pressure Measurements on Barnett Core. *SPE Reserv. Eval. Eng.* **2013**, *16*, 432–442. [CrossRef]
44. Saidian, M.; Kuila, U.; Prasad, M.; Lopez, L.A. A Comparison of Measurement Techniques for Porosity and Pore Size Distribution in Shales (Mudrocks): A Case Study of Haynesville, Eastern European Silurian, Niobrara, and Monterey Formations. In *AAPG Memoir 110: Imaging Unconventional Reservoir Pore Systems*; AAPG: Tulsa, OK, USA, 2016.
45. Katsube, T.J.; Scromeda, N.; Williamson, M. *Effective Porosity of Tight Shales from the Venture Gas Field, Offshore Nova Scotia*; Geological Survey of Canada: Ottawa, ON, Canada, 1992; pp. 111–119.
46. Rivera, S. *Ultrasonic and Low Field Nuclear Magnetic Resonance Study of Lower Monterey Formation: San Joaquin Basin*; Colorado School of Mines, Arthur Lakes Library: Golden, CO, USA, 2014.
47. Rivera, S.; Prasad, M. Effect of Mineralogy on NMR, Sonic, and Resitivity: A Case Study of the Monterey Formation. In Proceedings of the Unconventional Resources Technology Conference, Denver, CO, USA, 25–27 August 2014.
48. Carr, H.Y.; Purcell, E.M. Effects of Diffusion on Free Precession in Nuclear Magnetic Resonance Experiments. *Phys. Rev.* **1954**, *94*, 630–638. [CrossRef]
49. Kenyon, B.; Kleinberg, R.; Straley, C.; Gubelin, G.; Morriss, C. Nuclear magnetic resonance imaging—Technology for the 21st century. *Oilfield Rev.* **1995**, *7*, 19–33.
50. Meiboom, S.; Gill, D. Modified Spin-Echo Method for Measuring Nuclear Relaxation Times. *Sci. Instrum.* **1958**, *29*, 688. [CrossRef]
51. Washburn, E.W. Note on a Method of Determining the Distribution of Pore Sizes in a Porous Material. *Proc. Natl. Acad. Sci. USA* **1921**, *7*, 115–116. [CrossRef]

52. Prammer, M.; Drack, E.; Bouton, J.; Gardner, J.; Coates, G.; Chandler, R.; Miller, M. Measurements of Clay-Bound Water and Total Porosity by Magnetic Resonance Logging. *SPE* **1996**, *37*. [CrossRef]
53. Coates, G.R.; Galford, J.; Mardon, D.; Marschall, D. A new characterization of bulk-volume irreducible using magnetic resonance. *Log Anal.* **1998**, *39*, 1.
54. Clavier, C.; Coates, G.; Dumanoir, J. Theoretical and Experimental Bases for the Dual-Water Model for Interpretation of Shaly Sands. *Soc. Pet. Eng. J.* **1984**, *24*, 153–168. [CrossRef]
55. Yuan, Y.; Rezaee, R. Fractal analysis of the pore structure for clay bound water and potential gas storage in shales based on NMR and N2 gas adsorption. *J. Pet. Sci. Eng.* **2019**, *177*, 756–765. [CrossRef]
56. Tan, M.; Mao, K.; Song, X.; Yang, X.; Xu, J. NMR petrophysical interpretation method of gas shale based on core NMR experiment. *J. Pet. Sci. Eng.* **2015**, *136*, 100–111. [CrossRef]
57. Yuan, Y.; Rezaee, R.; Tongcheng, H.; Verrall, M.; Si-Yu, H.; Jie, Z. Pore Characterization and Fluid Distribution Assessment of Gas Shale. In Proceedings of the 80th EAGE Conference and Exhibition 2018, Unconventional Resources I (EAGE-SPE), Copenhagen, Denmark, 11 June 2018.
58. Bustin, R.M.; Bustin, A.M.; Cui, A.; Ross, D.; Pathi, V.M. Impact of shale properties on pore structure and storage characteristics. In Proceedings of the SPE Shale Gas Production Conference, Fort Worth, TX, USA, 16–18 November 2008.
59. Busch, A.; Schweinar, K.; Kampman, N.; Coorn, A.; Pipich, V.; Feoktystov, A.; Leu, L.; Amann-Hildenbrand, A.; Bertier, P. Shale Porosity—What Can We Learn from Different Methods. In *Fifth EAGE Shale Workshop*; EAGE: Catania, Italy, 2016.
60. Yuan, Y.; Rezaee, R. Impact of Paramagnetic Minerals on NMR-Converted Pore Size Distributions in Permian Carynginia Shales. *Energy Fuels* **2019**, *33*, 2880–2887. [CrossRef]
61. Suuberg, E.M.; Deevi, S.C.; Yun, Y. Elastic behaviour of coals studied by mercury porosimetry. *Fuel* **1995**, *74*, 1522–1530. [CrossRef]
62. Yao, Y.; Liu, D. Comparison of low-field NMR and mercury intrusion porosimetry in characterizing pore size distributions of coals. *Fuel* **2012**, *95*, 152–158. [CrossRef]
63. Melnichenko, Y.B.; Rupp, J.A.; Mastalerz, M.; He, L. Porosity of Coal and Shale: Insights from Gas Adsorption and SANS/USANS Techniques. *Energy Fuels* **2012**, *26*, 5109–5120.
64. Mastalerz, M.; Wei, L.; Drobniak, A.; Schimmelmann, A.; Schieber, J. Responses of specific surface area and micro- and mesopore characteristics of shale and coal to heating at elevated hydrostatic and lithostatic pressures. *Int. J. Coal Geol.* **2018**, *197*, 20–30. [CrossRef]